Increased Readiness for Water Splitting: NiO-Induced Weakening of Bonds in Water Molecules as Possible Cause of Ultra-Low Oxygen Evolution Potential

Tom Bookholt, Xian Qin, Bettina Lilli, Dirk Enke, Marten Huck, Danni Balkenhohl, Klara Rüwe, Julia Brune, Johann P. Klare, Karsten Küpper, Anja Schuster, Jenrik Bergjan, Martin Steinhart, Harald Gröger, Diemo Daum, and Helmut Schäfer*

The development of non-precious metal-based electrodes that actively and stably support the oxygen evolution reaction (OER) in water electrolysis systems remains a challenge, especially at low pH levels. The recently published study has conclusively shown that the addition of haematite to H_2SO_4 is a highly effective method of significantly reducing oxygen evolution overpotential and extending anode life. The far superior result is achieved by concentrating oxygen evolution centres on the oxide particles rather than on the electrode. However, unsatisfactory Faradaic efficiencies of the OER and hydrogen evolution reaction (HER) parts as well as the required high haematite load impede applicability and upscaling of this process. Here it is shown that the same performance is achieved with three times less metal oxide powder if NiO/H_2SO_4 suspensions are used along with stainless steel anodes. The reason for the enormous improvement in OER performance by adding NiO to the electrolyte is the weakening of the intramolecular O—H bond in the water molecules, which is under the direct influence of the nickel oxide suspended in the electrolyte. The manipulation of bonds in water molecules to increase the tendency of the water to split is a ground-breaking development, as shown in this first example.

1. Introduction

The ever-growing world population has serious negative consequences. On the one hand, overpopulation makes humanity more vulnerable to pandemics;[1] on the other hand, it drastically increases the production of greenhouse gases due to the growing number of farm animals and the increasing demand for electrical energy.[2] The highly efficient electrocatalytic splitting of water into hydrogen and oxygen, and its efficient conversion back to water in hydrogen fuel cells, is the most promising strategy for satisfying modern civilization's gigantic hunger for electrical energy in an ecological, i.e., carbon-neutral way.[3–8] The benefit of electrocatalytically initiated water splitting stands and falls with its efficiency, which in turn is directly determined by the sum of the overpotentials that occur at both electrodes at a technically reasonable current density.[3] Due to the sluggish

T. Bookholt, M. Huck, D. Balkenhohl, K. Rüwe, J. Brune, H. Schäfer
University of Osnabrück
The Electrochemical Energy and Catalysis Group
Barbarastrasse 7, 49076 Osnabrück, Germany
E-mail: helmut.schaefer@uos.de

X. Qin
Strait Institute of Flexible Electronics (SIFE Future Technologies)
Fujian Key Laboratory of Flexible Electronics
Fujian Normal University and Strait Laboratory of Flexible Electronics (SLoFE)
Fuzhou 350117, P. R. China

B. Lilli, D. Enke
University of Leipzig
Institute of Chemical Technology
04103 Leipzig, Germany

J. P. Klare, K. Küpper
University of Osnabrück Department of Physics
Barbarastrasse 7, 49076 Osnabrück, Germany

A. Schuster
University of Osnabrück
Inorganic Chemistry II
Barbarastrasse 7, 49076 Osnabrück, Germany

J. Bergjan, M. Steinhart
University of Osnabrück
Physical Chemistry
Barbarastrasse 7, 49076 Osnabrück, Germany

H. Gröger
Bielefeld University
Chair of Industrial Organic Chemistry and Biotechnology
Faculty of Chemistry
Universitätsstraße 25, 33615 Bielefeld, Germany

kinetics of the oxygen evolution reaction (OER), it is primarily the oxygen-evolving electrode that contributes to the cell overvoltage.[3]

In terms of large-scale practicality and adaptability to frequent changes in current load, electrodes that can withstand an acidic environment are advantageous; proton exchange membrane (PEM) electrolysis is considered the means of choice for renewable energy storage, characterized by high dynamics. However, this method relies on efficient electrodes that can withstand low pH conditions.[3] In addition, the overpotential at the OER electrode, which generally reaches higher values in acidic media than in alkaline media, is a problem.[9,10] Electrodes made of base metals in particular dissolve when positive potentials are applied in acidic media.[11] Compared to base metals, iridium oxide and ruthenium oxide, as well as IrO_2-RuO_2, have proven to be advantageous for the activity of electrocatalytically promoted OER in acids.[10–14] However, not least because of their scarcity and (consequently) high price, it would be attractive to replace these materials by more abundant and cheaper ones. Reducing the amount of expensive components (Ru or Ir) in the final electrode by simply adding more "common" elements is a reasonable and obvious approach to circumventing this problem.[15–18] However, all electrodes, even those containing noble elements such as ruthenium or iridium, are subject to significant mass loss when used as oxygen evolution electrodes in acidic media. For ternary Sr-Ir-O electrodes, significant leaching of Sr, together with smaller amounts of Ir, occurs when used as OER electrodes in acids.[19] Even at low current densities, $SrIrO_3$ was found to be acid-soluble.

In 2020 we introduced a method based on the use of a haematite/H_2SO_4 suspension instead of a clear acid electrolyte.[20] An extremely low potential of $\approx$1.26 V versus the reversible hydrogen electrode (RHE) was found at the Ni42 steel anode, resulting in a current density j of 30 mA cm^{-2}. More importantly, the low mass loss of the anode over 100 hours of operation is most likely due to the fact that the oxygen evolution centers are located on the metal oxide particles and not on the electrode. However, these significant advantages of the process come at the cost of serious disadvantages: The enormous amount of solids that have to be added to the acid (35 g per 125 ml of electrolyte, or 28% by weight) definitely limits the applicability of this strategy. A transfer of an approach based on such a high solid loading to common industrial processes seems almost impossible. In addition, the Faradaic efficiencies determined for the OER and hydrogen evolution reaction (HER) parts were not satisfactory. We have continued to work on the development of a water electrolysis concept that combines a very efficient anodic half-cell reaction based on ultra-low overpotentials for the OER with a reasonable mass loss of the non-noble metal-based anode.

Considering that currently all water electrolysis concepts based on transparent (clear) acidic electrolytes are accompanied by severe electrode wear and rather high overpotentials at reasonable current densities during operation, we have developed an approach using NiO/H_2SO_4 suspension electrolyte/Ni42 anode. It was found that by adding 10 g of NiO to 125 mL of 0.5 M H_2SO_4, the potential required to achieve a current density of 30 mA cm^{-2} could be reduced from $\approx$1.9 V versus RHE to 1.3 V versus RHE, a reduction of 600 mV. The mass loss of the Ni42 anode (200 mm^2 electrode area) when used for 50 000 s in 0.5 M H_2SO_4 at a current density of 30 mA cm^{-2} was 16 mg, corresponding to a weight loss of 6 µg mm^{-2} per hour of operation. This is a significant reduction compared to the corresponding value obtained in pure H_2SO_4-based electrolyte.

2. Results and Discussion

In order to demonstrate the effect of the addition of NiO to the electrolyte on the voltage-current behavior of the anode, water electrolysis was carried out in the simplest way possible from an experimental point of view, using a glass beaker (single compartment conditions, see Figure S1, Supporting Information).

However, for all experiments aimed at determining the total cell voltage, the Faraday efficiencies (method ii see below) and the electrode wear (weight loss of the anode) during operation, a home-built water electrolysis cell with a Nafion membrane was used, which realizes the separation of the half-cell compartments, as will be shown later.

Water splitting was first performed (for comparison) with a clear H_2SO_4 electrolyte and then repeated by adding NiO. The electrolysis was carried out in 0.5 M H_2SO_4 under strong stirring using a three-electrode set-up consisting of a Ni42 steel electrode used as anode (working electrode, WE), a platinum cathode (counter electrode, CE) and a RHE (positioned between WE and CE) used as reference electrode (RE). Activation of the electrode and the added metal oxide was ensured by performing a chronopotentiometry (CP) experiment based on a standardized current protocol known from previous experiments.[20]

The output value was 300 mA total current, corresponding to a current density of 150 mA cm^2 (electrode area: 2 cm^2). As expected, the potential required for this strong current flow was well above 2 V versus RHE (**Figure 1a**, blue curve). After 10 000 s the current density was reduced to 75 mA cm^{-2} and after a further 600 s to 30 mA cm^2. The current density was then held constant for 50 000 s, giving a total CP measurement time of 60 600 s (standard current protocol). As expected, the corresponding potential also gradually decreased, eventually reaching a constant value of $\approx$1.90 V versus RHE (j = 30 mA cm^{-2}), which is consistent with previous experiments.[11,20]

In a comparative experiment carried out under identical conditions (current-time settings of the CP measurement, stirring speed, temperature, electrodes and electrode arrangement), the clear electrolyte was replaced by a grey suspension of NiO in sulphuric acid (10 g NiO in 125 mL 0.5 M H_2SO_4). Then, after a period of 10 600 s (the current density was reduced to 30 mA cm^{-2}), the anode potential reaches a value of 1.27 V versus RHE. This is clearly different from the current/voltage behavior of the haematite/H_2SO_4-based electrolyte.[20]

An electrolyte based on haematite/H_2SO_4, with identical potentiostat settings, yields a CP curve that flattens out (after a running time of 10 600 s) and reaches an anode potential of 1.27 V versus RHE after $\approx$45 000 s.

D. Daum
Osnabrück University of Applied Sciences
Faculty of Agricultural Science and Landscape Architecture
Laboratory of Plant Nutrition and Chemistry
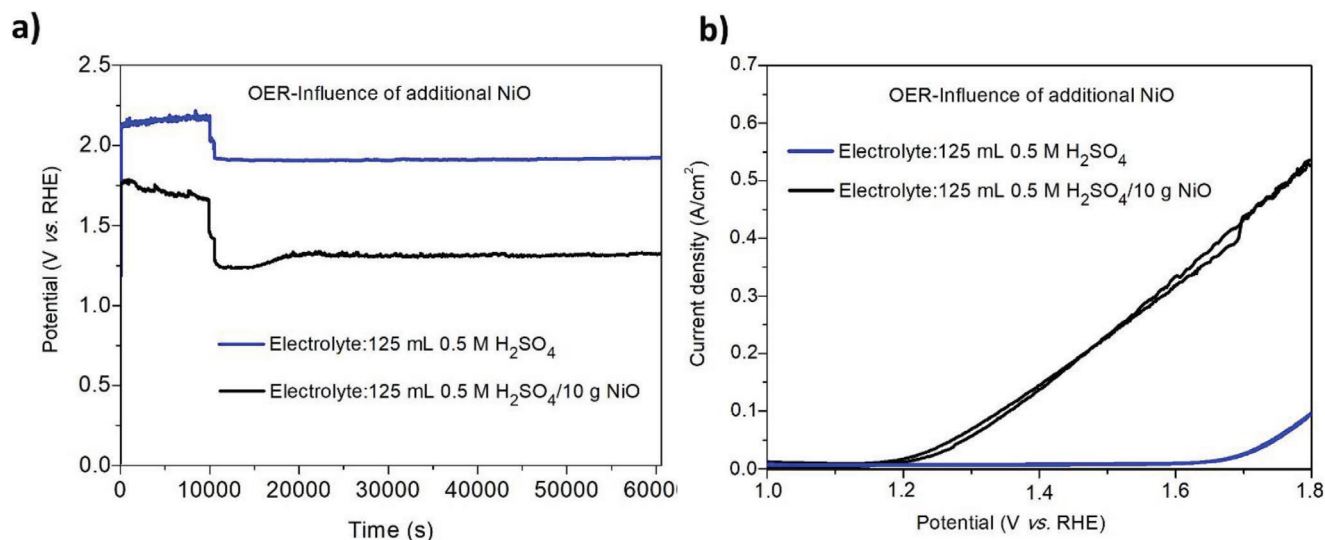Am Krümpel 31, 49090 Osnabrück, Germany

2310665 (2 of 14)

Figure 1. Voltage-current behavior of sulphuric acid-based electrolytes showing the effect of the NiO additive. a) CP measurements performed according to the standard current protocol (10 000 s at j = 150 mA cm^{-2}; 600 s at j = 75 mA cm^{-2}; 50 000 s at j = 30 mA cm^{-2}) with (black curve) or without (blue curve) NiO added to 0.5 M H$_2$SO$_4$. b) The results of cyclic voltammetry (CV) experiments performed with 0.5 M H$_2$SO$_4$ (blue curve); 125 mL 0.5 M H$_2$SO$_4$ + 10 g NiO (black curve). Scan rate: 20 mV s^{-1}. Electrode material: Ni42 steel. The CV derived from the suspension data was generated after 60 000 s CP according to the current standard protocol.

In Figure 1a, the CP experiment results (represented by the black curve) clearly demonstrate the significant impact of NiO on current voltage behavior, as revealed by the CP measurement. When the Ni42 anode was tested in a NiO/H$_2$SO$_4$ suspension electrolyte, the potential for the OER was notably lower than when tested in clear sulfuric acid (Figure 1a), regardless of the current density achieved during the experiment. When the operation time exceeded 20 000 s, both CP curves were parallel. However, the curve associated with the clear electrolyte was 590 mV higher than the curve obtained through electrolysis of the NiO/H$_2$SO$_4$ suspension. To achieve a current density of 30 mA cm^{-2}, a stable potential of ≈1.31 V versus RHE was needed with an electrolyte consisting of 125 mL 0.5 M H$_2$SO$_4$ and 10 g NiO. This resulted in an overpotential of only 81 mV for the OER at j = 30 mA cm^{-2}, which is an excellent low value.

In contrast, an OER potential lower than 1.229 V versus RHE was observed with haematite/sulfuric acid-suspension-based approach.[20]

Cobalt-based tool steel with lithiation-based activation showed excellent current/voltage behavior but for a brief time and lower current density.[21] Very recently, Najafpour et al. obtained overpotentials in the 100 mV range for OER in the alkaline regime.[22]

It has been discovered by Yang and co-workers that SrIrO$_3$, possessing a perovskite structure, exhibits a potential of 1.52 V versus RHE (≈300 mV) at a current density of 10 mA cm^2 in 0.5 M H$_2$SO$_4$.[23] Our system has an overpotential that is considerably lower than that of Ir-Sr-O-based systems, with a difference of at least five times.[24]

Samples for which the NiO/H$_2$SO$_4$ method was performed in this way (by adding 125 mL of 0.5 M H$_2$SO$_4$ to 10 g of NiO and performing CP according to the standard protocol) were subsequently designated as NiO@electro. A CV performed with NiO@electro is shown in Figure 1b (black curve). Experiments have shown that the process of oxygen evolution begins at a min-

imum potential of 1.24 V versus RHE and was not observed to occur at any lower threshold in this study. When a Ni42 anode is placed in a 0.5 M H$_2$SO$_4$ solution, the current density drops at a certain potential (as shown by the blue curve in Figure 1b). The absence of NiO therefore shifts the current-voltage curve by ≈450 mV toward higher voltages.

We varied not only the amount of NiO (between 6 mg and 20 g per 125 mL acid) but also the current protocol, the concentration and volume of sulphuric acid used and the stirring speed. An overview of all the experiments (59) carried out is given in Table S1 (Supporting Information). We performed a total of 16 polarization experiments, as shown in Figure 1a,b, using a standard composition of 125 mL of 0.5 M H$_2$SO$_4$/10 g NiO suspension. Although there were a few minor deviations, the current-voltage curves shown in Figure 1a,b are in fact representative of all 16 of the experiments. It was discovered that adding a specific amount of NiO to sulphuric acid is essential. If the amount of NiO (10 g added to 120 mL of 0.5 M H$_2$SO$_4$) is significantly decreased, the reduction of the overpotential of OER, as determined from CP tests (Figure 1a), cannot be sustained (Figure S2, Supporting Information). Strictly adhering to process parameters, including vessel dimensions, stirring speed, and stirring bar size, is crucial for consistent voltage-current performance and maximum reproducibility.

In some experiments, the platinum counter electrode was replaced with a Ni42 cathode, and it was found that this substitution had no impact on the potential of the anode half-cell for a considerable time. To comprehensively assess the efficiency of water electrolysis electrodes in generating hydrogen and oxygen, it is imperative to gauge the conversion rate of charge for each of these substances. There are two methods to determine the Faradaic efficiency (FE) of the OER. The first i) involves measuring the amount of O$_2$ that dissolves in the electrolyte during electrocatalysis using a fluorescence quenching method.[25] The
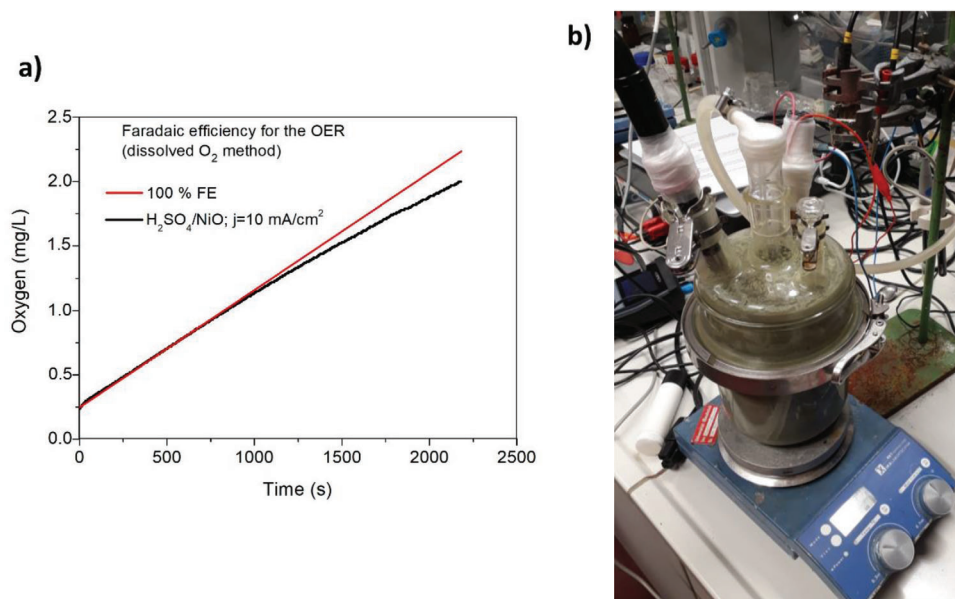
Figure 2. Determination of the FE of the OER based on the detection of dissolved oxygen. a) Faradaic efficiency measurements of the OER on Ni42 in a H_2SO_4/NiO suspension (black curve). Amount of electrolyte: 1.82 L; initial value of dissolved oxygen: 0.24 mg L^{-1} (t = 0 s). Electrode area: 2 cm^2; total current: 20 mA. The red line corresponds to 100% Faradaic efficiency with a line equation (exp. 1): y = 0.000911x + 0.24; line equation where y = oxygen concentration at 100% FE and x = running time. Faradaic efficiency of the OER after 2182 s run time: 88.5%. b) Photo of the apparatus used.

second method ii) involves collecting the O_2 gas and measuring its quantity.

Hydrogen gas is not significantly soluble in water, so the determination of the HER FE is limited to approach ii). **Figure 2** summarizes the results of detecting dissolved oxygen to determine the FE of the OER i).[25] The FE of OER on Ni42 electrode was measured in H_2SO_4/NiO electrolyte after 60 600 s of CP (see Figure 1a and Figure 2a).

The FE based on OER reached 88.5% after 2182 s of CP at a current density of 10 mA cm^{-2}.

This value was calculated assuming a two-electron process of direct water oxidation:

$H_2O \rightarrow H_2 + 0.5\ O_2$[20] (cf. the caption to Figure 2 and the experimental section for details). An important feature of this approach is that it measures the rate of oxygen evolution in a solution where the oxygen concentration is significantly lower than the saturation concentration (initial dissolved oxygen level: 0.24 mg L^{-1}). This is different from the second method which uses an electrolysis cell with a Nafion membrane to separate the anolyte and catholyte (shown in **Figure 3** and Video S1, Supporting Information), enabling the collection of both gases. In this method, oxygen is released from a solution that is already saturated with oxygen.

Video S1 (Supporting Information) shows the release of hydrogen and oxygen, from the pipes connected to the anode and cathode compartments' exits during electrolysis. **Table 1** exhibits the gas quantities gathered after a specific measurement period at a current of I = 300 mA (j = 150 mA cm^{-2}). The OER electrode's potential was 1.48 V versus RHE, with an overpotential of 251 mV (j = 150 mA cm^{-2}).
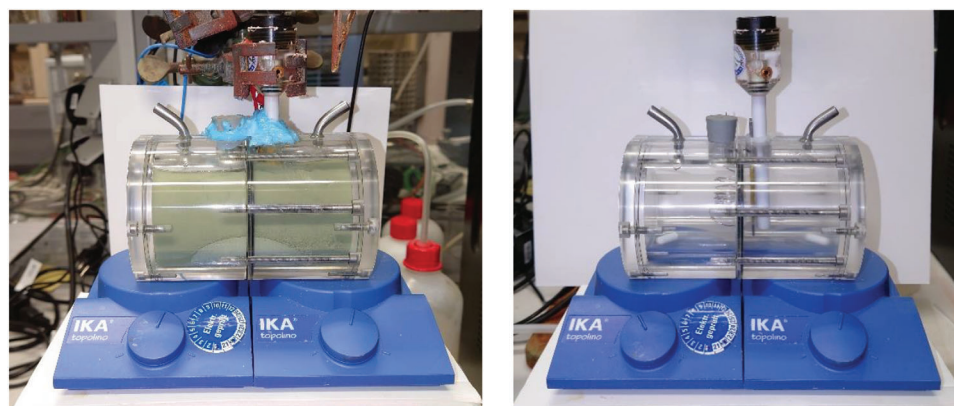

Figure 3. Photos of the homemade electrolysis cell. The photo on the left shows the cell filled with NiO/H_2SO_4 suspension. Dimensions: 12.5 × 8.2 × 7.5 cm (length x width x height); inner diameter: 5 cm; volume: 200 cm^3. Material: acrylic glass.

Table 1. The result of the determination of the Faradaic efficiency measurements based on the collection of the gases produced (method ii). Anolyte: 125 mL 0.5 M H_2SO_4 + 10 g NiO; Catholyte: 125 mL 0.5 M H_2SO_4 + 10 g NiO.

Measurement	Cell voltage [V vs RHE]	OER potential [V]	Tempera-ture [K]	Duration [s]	Volume O_2 [mL]	Volume H_2 [mL]	OER FE [%]	HER FE [%]
1 (j = 150 mA cm^{-2})	2.29	1.49	298	840	15.8	26.0	98.9	81.3
2 (j = 150 mA cm^{-2})	2.32	1.51	298	840	15.5	25.1	97.0	78.6
3 (j = 150 mA cm^{-2})	2.29	1.49	298	840	14.6	25.9	91.4	81.0

We have not been keeping the distance between the electrodes as small as possible, i.e., we have not achieved zero-gap conditions. However, by reducing the current density to 10 mA cm^{-2}, the cell voltage could be decreased to 1.35 V. Table 1 shows that the efficiency of the OER ranged from 91%–99%, whereas that of the HER was ≈80%. These findings were premised on the direct oxidation of water molecules, a two-electron process that yields H_2 and 0.5 O_2. Note that the Faradaic efficiency values for OER can differ slightly depending on the method used. (cf. Figure 2; FE: 88.5%). It is worth mentioning that Method ii used a much higher current density (150 mA cm^{-2}) compared to Method i (j = 10 mA cm^{-2}). Our previous works revealed significantly lower Faradaic efficiency values for OER and HER in haematite-based sulphuric acid electrolytes (HER: ≈53%; OER: ≈61%).[20]

Calculating the sum of overvoltage can provide valuable insight into the energy consumption and efficiency of an electrolyzer cell.[3] However, the electrodes are prone to significant wear and tear through material removal, resulting in increased maintenance and operating expenses. Anodes that are not made of platinum group metals, such as super duplex steel,[20] are particularly vulnerable to mass loss when operated in acids at high positive potentials. For instance, a Co-based steel anode was found to have lost ≈40 μg mm^{-2} following a CP test conducted at a constant low current density of j = 10 mA cm^{-2} for 50 000 s in diluted H_2SO_4 (0.05 M).[10]

The weight loss of the Ni42 electrode during the activation procedure was determined after 60 600 s of CP was completed using the standard current protocol (Figure 1a, black curve). The total mass deficit per electrode was ≈40 mg, equivalent to a weight loss of 0.2 mg mm^{-2} per area. Additionally, the electrolyte used underwent investigation using inductively coupled plasma optical emission spectrometry (ICP-OES), revealing the presence of Ni-, Fe-, Mn-, Cu-, and trace amounts of Zn ions (**Table 2**).

During the water electrolysis experiment utilizing 0.5 M H_2SO_4, it was observed that the Ni42 electrode (experimental part) experienced a mass reduction of 30.67 mg. This reduction was found to be equivalent to the combined mass of Ni, Fe, Mn, Cu, and Zn present in the electrolyte, which amounted to 30.47 mg. Furthermore, all ions found in the solution can be recognized as components of Ni42 steel. If NiO/H_2SO_4 suspension was utilized as the electrolyte, the total sum of ions collected in the electrolyte through ICP-OES (55.32 mg) surpasses the electrode's mass deficit (39.8 mg). The difference between these two values can be explained to some extent by the dissolution of the added NiO in sulphuric acid. A control experiment revealed that agitating 10 g of NiO in 125 mL of H_2SO_4 over a 48 h period led to the dissolution of 6.6 mg of NiO. This also explains why Ni is the dominant species found in solution (second row in Table 2).

However, most of the dissolved ions in the electrolyte originate from the partial dissolution of the electrode, which is different from our previous experimental finding where added haematite was the primary source of dissolved substance in H_2SO_4.[20] The question is to what extent dissolved material influences the active surface area of the steel electrode and the suspended NiO particles. SEM images (Figure S3, Supporting Information) of the steel electrode before and after its use as an anode in an electrolysis experiment (standard current protocol) show that the surface morphology of the metal surface has altered. However, the SEM images do not allow any conclusions to be drawn about a significant increase in the specific surface area. It has been found that the textural properties of NiO undergo a significant change upon electrolysis, as demonstrated by nitrogen sorption experiments (Figure S4, Supporting Information + experimental section). Whereas no specific surface can be attributed to unused NiO (0 m^2 g) the specific surface area (Brunauer-Emmet-Teller method[26]) of electrolyzed NiO amounted to 5 m^2 g. The increase in specific surface area results from the partial dissolution of the NiO particles in the H_2SO_4-containing electrolyte and reflects at least a "roughening" of the particle surface. This can also be seen by comparing the SEM images of used and unused NiO powder which show a finer fissured surface in the case of used NiO (Figure S5, Supporting Information). The particle size of NiO appears to be slightly reduced when subjected to electrolysis. This may also lead to the observed improved electrochemical

Table 2. Mass loss of the Ni42 electrode (column II) during the activation procedure (60000 s CP completed according to the standard current protocol) carried out in 125 mL of 0.5 M H_2SO_4, 125 mL of 0.5 M H_2SO_4 + 10 g NiO. Composition of the electrolyte used for activation (column III-VII).

Electrolyte	Mass deficit electrode	ICP OES results					
		Ni	Fe	Mn	Cu	Zn	Σ
125 mL 0.5 M H_2SO_4	30.67 mg	11.38 mg	18.75 mg	0.275 mg	0.06 mg	0.009 mg	30.47 mg
125 mL 0.5 M H_2SO_4 + 10 g NiO	39.8 mg	31.49 mg	17.99 mg	0.268 mg	0.022 mg	0.02 mg	49.79 mg

Table 3. Verification of the consumption of NiO solids during CP at a constant current density of $j = 30$ mA cm^{-2} (duration: 100 000 and 721 200 s).

Column I	Column II	Column III	Column IV	Column V	Column VI
Duration of the CP test (s)	Total electrolyte volume (mL)	Amount of NiO added to 250 mL of 0.5 M H$_2$SO$_4$ (g)	Weight loss of the electrode (mg)	Corrected total dry residue (g)	Difference between $\sum$ III +IV and column V (g)
100 000	250	20.0	33.4	19.9877	0.0457
721 200	250	20.0	231.7	20.2838	−0.0521

performance of the NiO-containing electrolyte compared to other systems (haematite/H$_2$SO$_4$ suspension).

In order to assess the wear of the anode and the consumption of NiO solids when used as an OER electrode at constant current density, complementary CP experiments were also started after completion of electrode/electrolyte activation. Thus, after completion of 60 600 s CP (Figure 1a, black curve), the anode was removed from the electrolyte, dried and weighed before CP testing (carried out in the electrolysis cell) continued (duration 100 000 and 721 200 s). In addition, the total dry residue was determined after the CP tests (duration 100 000 and 721 200 s) by drying the complete electrolyte (suspension consisting of 0.5 M H$_2$SO$_4$ + NiO solids) at 60 °C for three days under air. From that value the total dry residue of clear 0.5 M H$_2$SO$_4$ was subtracted resulting in the CTDR (corrected total dry electrolyte residue) see **Table 3**). It is clear from Table 3 that the amount of NiO used can be recovered in full at the end of the electrolysis process with differences of around ± 50 mg (column VI).

The weight loss of the Ni42 anode during long-term CP in the H$_2$SO$_4$/NiO suspension at a constant current density of $j = 30$ mA cm^{-2} was ≈6 μg mm^{-2} per hour of operation (total mass loss: 33.4 mg while 100 000 s), 5.78 μg mm^{-1} per hour of operation (total mass loss:231.7 mg while 721 200 s respectively. The CP plot of the long-term measurement (t = 721 200 s) is shown in Figure S6 (Supporting Information). Considering the high current density, the aggressive medium (pH 0) and, in particular, the fact that the anode is composed exclusively of non-platinum group elements, this is a very good result. This, together with the electrochemical performance (low overpotentials), demonstrates the effectiveness of this strategy. For comparison, untreated Ni42 steel shows a mass loss of ≈14 μg mm^{-2} per operating hour[11] when used as an anode for water electrolysis in 0.05 M H$_2$SO$_4$ at a current density of only 10 mA cm^2. In addition to the above-mentioned shift of oxygen generation centers from the electrode to the particles, the saturation of the solution with Ni^{2+} ions caused by the addition of NiO to the electrolyte could also be a reason for the lower material removal at the anode. When an (untreated) Ni42 anode is used in pure 0.5 M H$_2$SO$_4$ at a current density of 30 mA cm^{-2}, a mass loss of 122.7 μg mm^{-2} per operating hour occurs (total mass loss of the electrode during 50 000 s of CP testing: 340.7 mg; Figure S7, Supporting Information), which is more than 20 times higher. Even noble metal oxygen-evolving electrodes suffer a significant mass loss during operation in acidic media. For example, Yang et al. investigated 6H-phase SrIrO$_3$ as an OER electrode in 0.5 M H$_2$SO$_4$ at a current density of $j = 10$ mA cm^{-2}. Although it performed better than IrO$_2$, a certain amount of leached Ir was detected in the electrolyte by ICP-OES. Studies on Co$_3$O$_4$ films,[27] RuFeOx,[28]

SrRuO$_3$[30] and Ir$_{0.08}$Co$_{2.92}$O$_4$[29] report either acceptable low over-potentials ($\eta = 160$ mV,[30] $\eta = 187$ mV[28]) or quite low leaching. However, on the one hand, the current densities reported were rather low ($j = 10$ mA cm^{-2},[28–30] 1 mA cm^{-2}[27]) and on the other hand, they lack Faradaic efficiency tests. As we have shown in our previous report, assessing performance without quantifying the amount of oxygen gas produced carries many risks and can be misleading, especially when OER is intended in the acidic range (**Figure 4** in ref. [20]).

Proton transfer and long-term stability of the proton exchange membrane (PEM) can be affected by the electrolyte containing the active metal elements. However, as can be seen in Figure S6 (Supporting Information), the potential required to achieve a current density of 30 mA cm^{-2} did not increase during the measurement period, suggesting no change in the proton transfer capabilities of the membrane, which showed no visible signs of damage (Figure S8, Supporting Information). Atomic force microscopy (AFM) experiments also showed no differences between the used and unused membranes. (Figure S9, Supporting Information).

The XPS spectroscopic study includes powder samples of unused NiO, denoted as NiO, and the solid residue of the NiO@electro sample (from NiO/H$_2$SO$_4$ electrolysis experiments; standard composition/standard current protocol) dried in air atmosphere at 313 K for 30 h, denoted as NiO@electro dry, as well as the study of the electrode. Figure 4a shows the Ni 2p$_{3/2}$ spectra of the NiO and NiO@electro dry samples, as well as two different positions on the Ni42 electrode after being used as the WE in NiO/H$_2$SO$_4$ electrolysis experiments according to the standard current protocol. The Ni 2p$_{3/2}$ spectra of the NiO@electro dry and NiO samples contain two maxima located at 854.6 and 856.2 eV. The first peak can be attributed to divalent Ni states, probably originating from oxidic species such as NiO or NiFe$_2$O$_4$. The peak at 856.2 eV can be attributed to either γ-NiOOH (Ni^{3+}) or Ni(OH)$_2$ (Ni^{2+}), which cannot be clearly distinguished by the Ni 2p$_{3/2}$ binding energy.

However, considering additional electron paramagnetic resonance (EPR) results (Figure S10 see EPR results below, Supporting Information), we assume that this peak can be attributed to Ni^{3+} in a crystalline environment. Compared to unused NiO, it is noteworthy that NiO@electro dry contains a higher proportion of Ni^{3+}, which is to be expected given the oxidative potentials prevailing at the anode. The Ni 2p$_{3/2}$ spectra recorded at two different positions of the WE consist of two features at 852.6 eV, indicating some metallic nickel, and a main peak at 856.2 eV, which can be attributed to either γ-NiOOH (Ni^{3+}) or Ni(OH)$_2$ (Ni^{2+}). This is a finding worth looking at more closely. In 2016, we reported on the use of Ni42 steel as a proposed anode for water electrolysis in alkaline media. Ni42, when used as a water oxidation electrode in
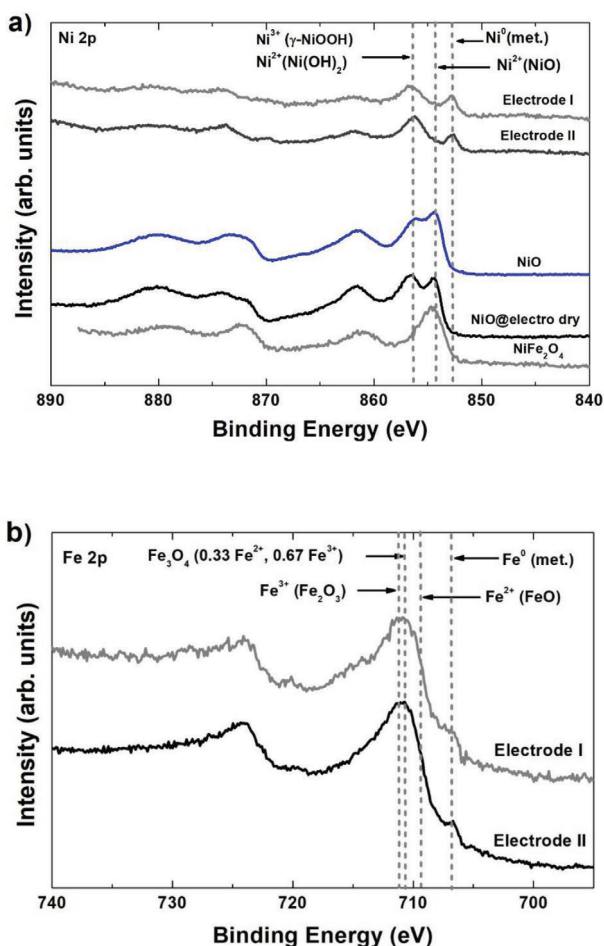
Figure 4. X-ray photoelectron spectroscopy (XPS) results. Figure 4a: Ni 2p XPS results of NiO@electro dry, NiO, Electrode I and Electrode II samples together with a reference spectrum of NiFe$_2$O$_4$.[31] The vertical lines indicate the Ni 2p$_{3/2}$ binding energies of metallic nickel, Ni^{2+} ions in oxides (NiO or NiFe$_2$O$_4$) and of γ-NiOOH and Ni(OH)$_2$ as a guide to the eye.[32–34] Figure 4b: Fe 2p core level spectra of samples 9 and 10 along with vertical lines indicating the Fe 2p$_{3/2}$ binding energies of metallic Fe, FeO, Fe$_3$O$_4$, and Fe$_2$O$_3$ as a guide to the eye.[31].

clear electrolytes, showed no metallic nickel or metallic Fe content on the surface, as revealed by XPS experiments.[35] However, in our first suspension-based approach using haematite/H$_2$SO$_4$ mixtures XPS experiments performed on Ni42 electrodes used as anodes in water electrolysis experiments revealed a high proportion of metallic fractions of nickel and iron.[20] For example, we proposed a reduction of Ni^{3+} (produced by an oxidation process at positive potentials at the anode) by magnetite particles upon collision with the electrode via a mechanochemical reaction.[20] With this in mind, our new research suggests that when NiO/H$_2$SO$_4$ suspensions are used as electrolytes in water electrolysis, NiO particles obviously reduce Ni^{3+} or Fe^{3+} (produced by an oxidation process at positive potentials at the anode) back to metallic nickel or iron (see below) via a mechano-chemical reaction. More recently, nickel-based intermediates and the mechanism of OER in alkaline media have been investigated using operando spec-

troscopic tools by Lee et al.[36] It was found that starting from Ni(OH)2, 2-e oxidation does indeed lead to a Ni(III)-O species.

Figure 4b shows the Fe 2p core level spectra recorded at two different positions of the Ni42 electrode after it was used as a WE in NiO/H$_2$SO$_4$ electrolysis experiments. Besides a small contribution of metallic states, the maximum intensity is located at 710.8 eV, indicating a dominant amount of Fe^{3+} ions at the surfaces of the electrode. The presence of the charge transfer satellite at 719.8 eV also indicates that the majority of Fe ions are trivalent. A small amount of Fe^{2+} (lower than in Fe$_3$O$_4$) cannot be completely excluded. On the other hand, the presence of FeOOH can be rather excluded since the Fe 2p$_{3/2}$ binding energy of FeOOH is expected to be at higher binding energies ≈711.8 eV.[37]

EPR spectroscopy was performed at 296 and 15 K in the X-band (≈9.5 GHz) on the NiO and NiO@electro dry samples (Figure S10, Supporting Information). The experimental EPR spectra recorded at 296 K for both samples are similar to those reported for pure NiO nanoparticles[38] and mixed lithium-nickel oxides.[39] The spectra for NiO and NiO@electro dry are characterised by very broad, asymmetric EPR lines, which also differ significantly regarding their g-values (NiO: ≈3.8, NiO@electro dry: ≈2.7), linewidth ΔB (NiO: ≈310 mT, NiO@electro dry: ≈180 mT) and spectral symmetry. In the case of NiO nanoparticles obtained by urea-based combustion, the changes in g and line width were explained by different porosities of the NiO powders.

Spectra recorded at 15 K (Figure S10, Supporting Information) show more complex features throughout the B-field region and also differ significantly between NiO and NiO@electro dry. The spectrum of the NiO sample shows some broad overlapping features and a narrow signal (ΔB ≈19 mT) at g ≈2.07. The spectrum of NiO@electro dry shows a similar "background" of broad lines and an additional clear signal at g ≈4.6 in addition to the g ≈2.07 resonance also observed for this sample. Similar broad overlapping features, i.e., broadening of the EPR signal observed at 296 K and splitting into several components, have also been observed for mixed lithium-nickel oxides at lower temperatures (150 K),[39] where they have been attributed to Ni^{3+} ions being either in the low spin (S = 1/2)[40–43] or in the high-spin (S = 3/2) state.[44,45]

Therefore, based on these findings and the XPS results, we assume that some of the Ni is present in the 3+ oxidation state, i.e., that Ni^{3+} ions are likely to be present in the crystalline environment. The results of the XPS and EPR studies may give a homogeneous picture, but they do not explain the very low overpotential we have determined for the OER.

2.1. The Origin of the Unusually High Electrocatalytic Activity

In our previous report on suspension electrolytes, we concluded that water splitting was highly efficiently catalyzed by the haematite-based particles.[20] A fundamental clue to this theory was that no consumption of haematite could be detected during electrolysis. Replacing the haematite with NiO gave the same result (Table 3 and Table S2, Supporting Information).

After polarization for 60 600 s (activation for 60 600 s of CP according to the standard current protocol), the electrolysis was stopped, and the suspension was centrifuged. After washing with
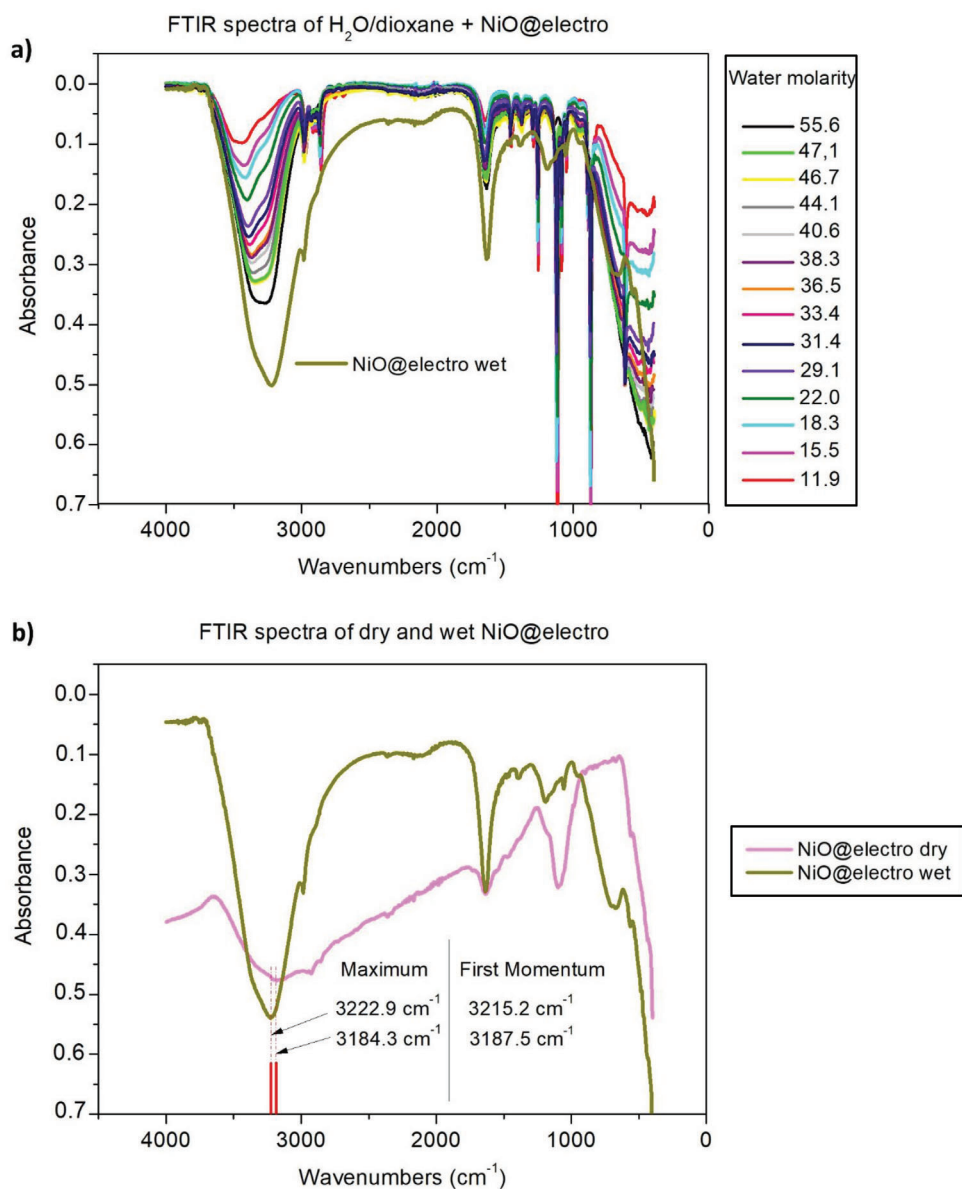
ADVANCED
SCIENCE NEWS
www.advancedsciencenews.com

NANO · MICRO
small
www.small-journal.com

Figure 5. The results of the FTIR spectroscopy experiments. a) FTIR spectra of water/dioxane solutions; and FTIR spectrum of the wet residue of the NiO@electro sample. Absorbance versus wave number plot. b) FTIR spectra of dry and wet NiO@electro. Absorbance versus wave number plot. The maximum of the O-H stretching frequency is shown in the graph. First moment of O-H stretching frequency: 3215.2 cm^{-1} (NiO@electro wet); 3187.5 cm^{-1} (NiO@electro dry).

water and drying in air at 333 K for 24 h, the weight of the residue and the electrode was determined. In addition, ICP-OES analysis of the electrolyte was performed. The detailed results (Table S2, Supporting Information) confirmed that there was indeed no consumption of NiO during polarization in H_2SO_4. The same applies (see text above and Table 3) for CP tests at constant current density. The ultra-low overpotential for water oxidation, which can be derived from electrochemical measurements covering both steady–state (Figure 1a) and quasi–steady–state conditions (Figure 1b), was only obtained when NiO was added to the clear acidic electrolyte. Therefore, an explanatory theory in which NiO or secondary products formed from NiO play a major role is sought.

Vibrational spectroscopy is known to be a powerful tool for studying the microscopic structure of water, i.e., the molecular structure as well as the cooperative hydrogen bonding network.[46,47]

As we have shown elsewhere in a report dealing with infrared spectroscopic analysis of aqueous solutions, the position of the O-H stretching mode is a descriptor of the O-H bond strength (intramolecular bonding), which in turn has a significant effect on the key data of the OER.[48] **Figure 5a** shows the FTIR spectra of water/1,4-dioxane solutions (water molarities between 11.9 and 55.5 mol L^{-1}). It can be clearly seen that the stretching vibration is shifted by 175 cm^{-1} to higher frequencies (blue shift) with increasing dioxane content (55.6 mol H_2O/L:3265 cm^{-1}; 11.9 mol
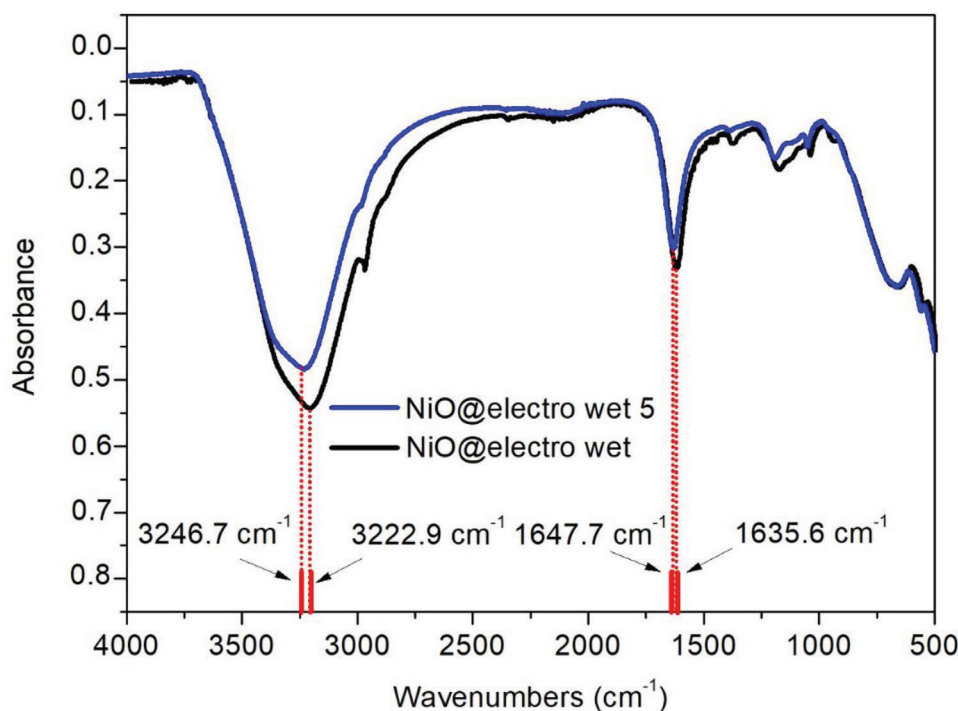
Figure 6. FTIR spectra of the wet residue of electrolysis experiments performed with 125 mL 0.5 M H_2SO_4 + 10 g of NiO (NiO@electro wet) and with 125 mL 0.5 M H_2SO_4 + 5 g of NiO (NiO@electro wet 5). The maximum absorption occurs at wave numbers of 3222.9 and 1635.6 cm^{-1} (NiO@electro wet) and at wavenumbers of 3246.7 and 1647.7 cm^{-1} (NiO@electro wet 5).

H_2O /L:3440 cm^{-1}). We have shown that this phenomenon is accompanied by a significant increase in the OER onset potential as derived from CV experiments.[48]

These results have now been combined with the FTIR spectrum of the post-electrolytic NiO residue. In addition to NiO@electro dry, another sample was prepared with a higher water content than NiO@electro dry, designated NiO@electro wet, as the water content of this (post-electrolytic) NiO residue has a significant effect on the FTIR spectrum. NiO@electro wet was obtained by drying the freshly centrifuged NiO residue (standard composition and standard current protocol) at room temperature for 1 hour. Figure 5a shows the combined FTIR results.

The absorption band of the O-H stretching vibration in the FTIR spectrum of the NiO@electro wet sample shows the lowest frequency with a maximum at 3222.9 cm^{-1} among all the spectra shown in Figure 5a. We emphasize that the position of the O-H stretching of NiO@electro wet (3222.9 cm^{-1}) is significantly red-shifted even compared to the O-H stretching of a pure aqueous solution (3265.3 cm^{-1}; molarity: 55.6 mol H_2O/L). Thus, there is a fundamental reason to conclude that the intramolecular O-H bond of those water molecules that are tightly bound to the residue of the sample NiO@electro is weakened. Upon electrolysis Ni ions (which were detected in the electrolyte) intensify this effect which goes hand in hand with an increase in the specific surface area as confirmed by nitrogen physisorption (Figure S4, Supporting Information).

This becomes even clearer when considering the FTIR spectrum of the sample NiO@electro dried under air atmosphere at 313 K for 30 h, denoted as NiO@electro dry (Figure 5b). The absorption band in the FTIR spectrum of the NiO@electro dry sample, which can be attributed to the stretching of the intramolecular O—H bond, is clearly red-shifted (3184.3 cm^{-1}) compared to the corresponding region of the FTIR curve recorded with the NiO@electro wet sample (3222.9 cm^{-1}). When the NiO@electro dry sample was subjected to the FTIR experiment, obviously more H_2O molecules were detected among those affected by NiO. This, in our opinion, explains the stronger red shift of the O-H stretching vibration in the FTIR spectrum recorded with the NiO@electro dry sample and sheds light on the determination of the origin of the high OER efficiency of the NiO@electro sample. However, this can only serve as an explanation if one considers that in suspension-based approaches, unlike clear electrolytes, the oxygen evolution centers are not located on the surface of the electrode but on the surface of the suspended particles.[20] As a direct consequence, it's not the bulk water that is split into its decomposition products, but the H_2O molecules firmly attached to the suspended NiO. In order to clarify why a certain amount of NiO is crucial for the desired reduction of the OER overpotential, we additionally examined the experiment carried out with 5 g NiO/125 mL 0.5 M H_2SO_4 (sample NiO@electro wet 5) using FTIR spectroscopy. In fact, both the O-H stretching and O-H bending vibrations are not as clearly redshifted as shown in the FTIR spectrum derived from the standard composition experiment (sample NiO@electro wet), the comparison of which is shown in **Figure 6**.

To shed more light on what actually happens to the transition metal oxide during the CP-based activation process, we performed additional FTIR studies on metal oxide-based residues. We studied NiO simply stirred in sulphuric acid (10 g NiO in 125 mL 0.5 M H_2SO_4) for 45 min to simulate the actual state
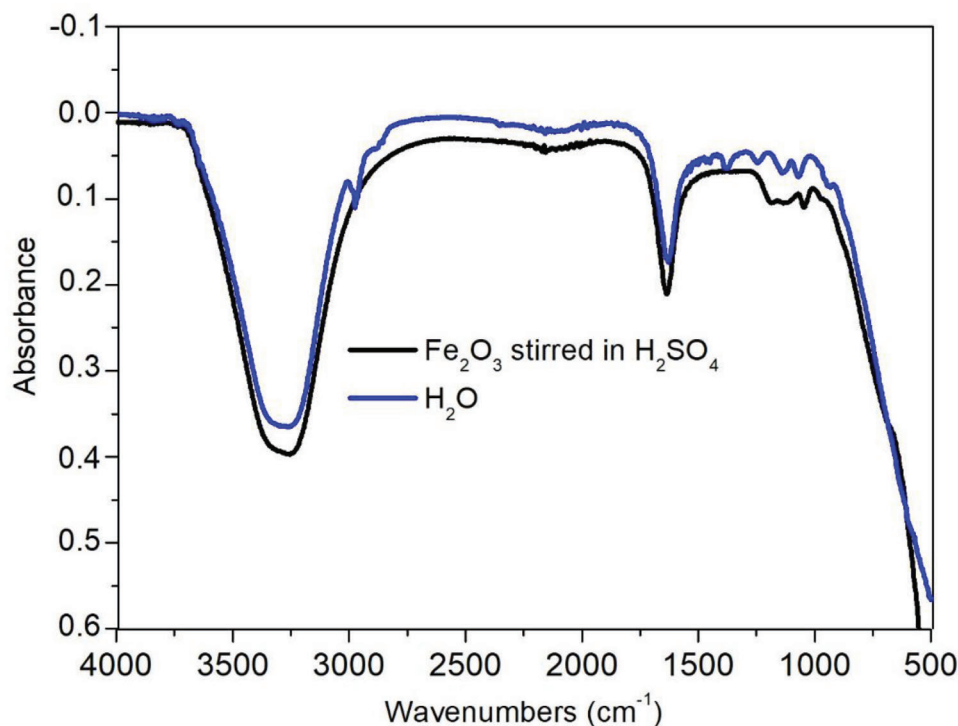
**ADVANCED
SCIENCE NEWS**
www.advancedsciencenews.com

**NANO · MICRO
small**
www.small-journal.com

Figure 7. FTIR spectra of haematite in sulphuric acid (35 g Fe_2O_3 in 125 mL 0.5 M H_2SO_4) stirred for 45 min.

in the metal oxide at the start of the electrolysis. As can be seen from Figure S11 (Supporting Information), a weak red shift of both (O-H stretching + bending) vibrations was obtained. This explains why a certain reduction of the OER overpotential with the addition of NiO is already visible at the beginning of the CP experiment (Figure 1a, black curve). However, it should be noted that the reduction in the stretching mode vibrational frequency (from 3265.3 to 3248.1 cm^{-1}) is much weaker than that obtained with the electrolyte at the end of the activation process (Figure 5). This agrees with the results of the nitrogen physisorption experiments, which show that a significant increase in specific surface area is only obtained for NiO samples subjected to electrolysis (Figure S4, Supporting Information).

This applies all the more to experiments carried out with haematite/H_2SO_4. When haematite is added to H_2SO_4, an excellent low OER potential (1.27 V *vs*. RHE at j = 30 mA cm^{-2} current density) can only be obtained after a run time of ≈45 000 s, whereas the OER potential obtained subsequently after the addition of haematite remains unchanged.[20] The current-voltage behavior (observed in the CP experiment) changes with time and these differences should also be reflected in different FTIR spectra.

FTIR experiments carried out on the residue of the electrolysis of 35 g of haematite in 120 mL of 0.5 M sulphuric acid according to the standard current protocol (sample Fe_2O_3@electro) showed an O-H stretching band positioned at 3239.0 cm^{-1} which is red-shifted when compared with bulk water (Figure S12, Supporting Information). In addition, the absorption band that should be assigned to the O-H bent mode (maximum of absorption at 1629 cm^{-1}) is red-shifted compared to bulk water (1636 cm^{-1}; Figure S12, Supporting Information).[48] The pic-

ture was similar to that obtained after electrolysis of NiO/H_2SO_4 (Figure 5a).

However, the simple stirring of haematite with sulphuric acid resulted in an FTIR spectrum that was indistinguishable from that of water, i.e., there was no shift in the typical absorption bands of water molecules as seen after completion of the electrolysis (**Figure 7**). Only when the Fe_2O_3/H_2SO_4 mixture was subjected to prolonged electrolysis did a spectrum emerge similar to that seen in the NiO/H_2SO_4 experiments, with the absorption bands of water shifted to lower wavenumbers. These results are yet another demonstration of how powerful FTIR spectroscopy can be in predicting the expected OER potential of different electrolyte systems. This outcome suggests that the reason for the significant reduction in OER overvoltage when NiO is used as an additive is due to the lengthening of the intramolecular O-H bonds in the water molecules under the direct influence of NiO.

Additionally, to understand how NiO particles affect the strength of O─H bonds in water molecules, we carried out spin-polarized first-principles calculations based on density functional theory (DFT). Interactions between particle surfaces and water molecules were investigated on the stable (100) and (110) facets of the cubic NiO crystal (**Figure 8**).[49]

The NiO-H_2O binding strength was calculated according to

$$E_b = E\left(NiO - H_2O\right) - \left[E\left(NiO\right) + E\left(H_2O\right)\right] \qquad (1)$$

where E(NiO-H_2O), E(NiO), and E(H_2O) are the energies of the adsorbed system, NiO slab, and isolated water molecule, respectively. The calculated binding energies for water molecules adsorbed on the (100) and (110) are 0.4 and 1.47 eV, respectively, with corresponding binding densities of 5.7 and 4.04 molecules
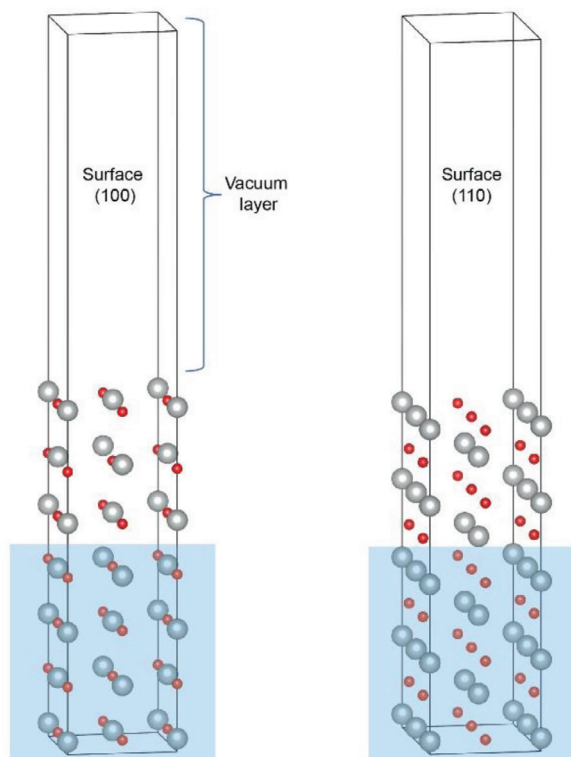
**ADVANCED
SCIENCE NEWS**

www.advancedsciencenews.com

**NANO · MICRO
small**

www.small-journal.com

Figure 8. Slab models for the (100) and (110) of NiO particles. Silver and red balls denote Ni and O atoms, respectively. Atoms in blue areas were fixed to mimic the center part of the NiO particles.
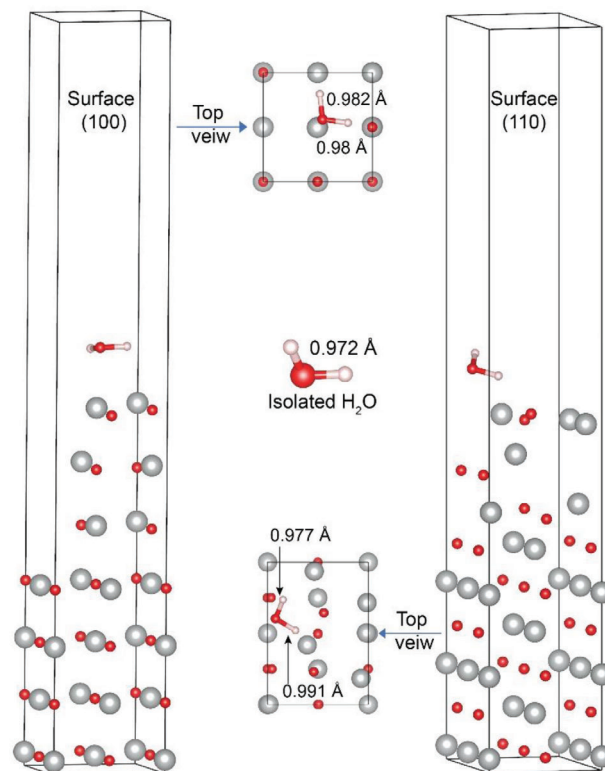

Figure 9. Optimized $NiO-H_2O$ systems. Silver, red, and pink balls denote Ni, O, and H atoms, respectively.

nm^2. By examining the optimized atomic structures, we found that the O—H bonds of water molecules elongate upon adsorption compared with those of isolated molecules (**Figure 9**). These findings imply that the interaction between NiO particles and water molecules leads to a weakening of the O—H bonds, aligning with the infrared spectroscopic measurements.

Our strategy to manipulate the bonds in the water molecules to increase the tendency of the water to split and thus improve the efficiency of water electrolysis is the first of its kind.

Other strategies (not based on improving the readiness of water molecules to split, but rather on improving the electronic structure of Ni-based OER electrocatalysts to enhance the catalytic properties have been developed by several groups.[50–61]

NiO-based OER electrocatalysts were activated upon regulating the electronic structure of NiO as was recently demonstrated by Lyu et al.[54]

3D nickel-iron phosphides nanosheets modified by MnO_x nanoparticles grown on nickel foam (MnO_x/NiFeP/NF) were recently found to have advanced OER electrocatalytic properties[55] and ferric/molybdate (Fe^{3+}/MoO_4^{2-}) co-doping strategy was reported to promote the OER activity of Ni oxyhydroxide.[56]

3. Conclusions

A very low anode potential (j = 30 mA cm^{-2}, 1.31 V versus RHE) during water electrolysis was obtained when NiO was suspended in H_2SO_4-based electrolyte. We assume that the oxygen evolution centers are located on the suspended NiO particles and that

water molecules tightly bound to the suspended NiO are split. FTIR spectroscopy proved to be an ideal descriptor of the readiness of water molecules to split into hydrogen and oxygen. Based on the FTIR results, we concluded that the origin of the enormous increase in OER performance when using NiO as an additive was due to the weakening of the intramolecular O—H bonds in the water molecules under the direct influence of the nickel oxide suspended in the electrolyte. This was also confirmed by DFT-based first-principles calculations. This can be seen as the first example of tailor-made manipulation of the bonds in water molecules in a typical electrolyte for water electrolysis (H_2SO_4), with the aim of improving the efficiency of water splitting without changing the electrodes.

4. Experimental Section

FTIR Measurements: FTIR measurements of dioxane/water mixtures and NiO@electro wet and NiO@electro dry samples were performed on a Bruker Vertex 70 FTIR spectrometer equipped with an ATR unit. The IR spectra were recorded with a resolution of 2 cm^{-1} in the spectral range 400–4000 cm^{-1}.

Calculation of the first momentum of frequency: For each dataset, two position parameters were computed by the maximum of the transmittance f and by its first normalized moment

$\int_\Omega x f(x) dx / \int_\Omega f(x) dx$ where we restricted to the field of view $\Omega = [3020, 3700]$.

Samples of NiO@electro wet and NiO@electro dry were prepared according to the following procedure: Both samples were obtained at the end of the CP standard current protocol carried out with the NiO/H_2SO_4

(10 g NiO/125 mL 0.5 M H_2SO_4) electrolyte. The residue obtained by centrifuging the electrolyte (sample NiO@electro) was washed with water and dried in air at room temperature for 1 h (still wet), referred to as sample NiO@electro wet. Drying of the sample NiO@electro wet under air at 318 K for 16 h resulted in the sample referred to as NiO@electro dry.

ICP OES Measurements: The solution samples were analyzed by inductively coupled plasma optical emission spectrometry (ICP-OES, iCAP 7400 Duo equipped with MiraMist Teflon nebulizer, Thermo Fisher Scientific Germany BV & Co KG) according to DIN EN ISO 11885:2009-09. Concentrations of selected elements were determined at wavelengths of 324.750 nm (Cu) and 206.200 nm (Zn) by using the axial view mode, and at wavelengths of 221.647 nm (Ni), 259.940 nm (Fe) and 257.610 nm (Mn) by using the radial view mode. The calibration standards were prepared according to the matrix of the analyte solution and contained 1–25 mg L^{-1} of the determined elements, in up to four gradations, depending on the expected concentration range.

XPS Spectroscopy Measurements: The experiments were performed using a PHI Versaprobe III spectrometer equipped with a monochromatic Al Kα, micro-focused scanning X-ray source. For the current measurements, the X-ray beam size was set to 100 µm. A dual beam charge neutralisation method was used to compensate for charging effects. The overall resolution of the spectrometer is 1.5% of the analyser pass energy, in this case 0.45 eV. The spectra were calibrated to the common binding energy scale by shifting the C 1s line to 284.8 eV, the binding energy of the C—C bond.

EPR Measurements: Continuous wave (cw) EPR measurements were performed on a Bruker Elexsys E580 EPR spectrometer operating at X-band (≈9.4 GHz), equipped with a Bruker SHQ Super High Sensitivity Probehead (Bruker Biospin; Germany). EPR spectra were recorded at 15 and 296 K. An Oxford ESR900 continuous flow cryostat (Oxford Instruments, Oxfordshire, UK) and a temperature controller (ITC 3; Oxford Instruments) were used to stabilise the sample temperature. The EPR spectra were obtained using a sweep time of 83 s with a time constant of 20.48 ms, a field modulation amplitude of 5 G, a modulation frequency of 100 kHz and 1 mW microwave power. The scan range was 6000 Gauss, centred at 3050 Gauss. The powder samples were filled into EPR quartz capillaries of 3 mm internal diameter.

Electron Microscopic Experiments: The surface morphology of the Ni42 electrodes was characterized by a Zeiss EVO MA 10 Scanning Electron Microscopy (SEM) equipped with an Oxford Inca Energy 250 Energy-dispersive X-ray spectroscopy (EDS) device.

AFM Experiments: AFM measurements were performed in contact mode on an NT-MDT model NTEGRA Probe NanoLaboratory. The V-shaped cantilevers had nominal lengths of 140 µm, force constants of 0.2 Nm^{-1} and a resonant frequency of 13 kHz. The tip radius was 10 nm. The AFM images were processed using the Nova Px.

Determination of the Specific Surface Area: Nitrogen sorption isotherms were measured at 77 K using a SURFER (Thermo Fisher Scientific). Before the measurements, the samples were outgassed under vacuum for 10 h at 523 k. The specific surface areas were determined with the method of Brunauer-Emmet-Teller (BET)[26] according to DIN ISO 9277.[62] The total pore volume was calculated at p/p$_0$ = 0.995.

Electrochemical Measurements: A three-electrode setup was used for all CV and CP measurements. A RHE (HydroFlex, Gaskatel Gesellschaft für Gassysteme durch Katalyse und Elektrochemie mbH. 34127 Kassel, Germany) was used as the reference standard, therefore all voltages are given against this reference electrode (RE). No compensation for the IR voltage drop was provided.

The working electrode (WE) was made of Ni 42 steel (Schmiedetechnik Faulenbach, Wiehl, Germany) with a total geometry of $100 \times 10 \times 1.5$ mm, on which an apparent surface of 2 cm^2 was defined by an insulating tape (Kapton tape). Pre-treatment: Prior to electrolysis, the metal surface was intensively cleaned with ethanol and polished with 600-grit SiC paper. The surface was then intensively rinsed with deionized water and dried in air for 5 h. The weight was determined using a precision balance (Sartorius 1712, 0.01 mg accuracy) before polarization.

A Pt wire electrode (Evochem Advanced Materials GmbH, Offenbach am Main, Germany) (4×5 cm geometric area) was used as the counter electrode (CE). For all measurements, the RE was placed between the

WE and the CE. The measurements were performed at room temperature (295.15 K) in a 150 mL glass beaker (inner diameter: 55 mm; height: 80 mm) when the measurements were aimed at determining the voltage-current behaviour of the anode. A home-built water electrolysis cell with a Nafion membrane Nafion NM-212; 50.8 µm thickness (Quintech, Danziger Straße 8, 73035 Göppingen, Germany), which realizes the separation of the half-cell compartments, was used for all experiments aimed at determining the total cell voltage as well as the Faradaic efficiency according to method ii (Figure 3).

The distance between the WE and the RE was set to 2 mm and the distance between the RE and the CE was set to 2 mm. The electrolyte was prepared using 125 mL of 0.5 M H_2SO_4 (VWR, Darmstadt, Germany) to which 10 g NiO (97% purity; CAS: 1313-99-1; Thermo Fisher Scientific, Waltham, Massachusetts, USA) was added under stirring. Both compartments of the electrolysis cell were filled with separately activated H_2SO_4/NiO mixtures, see method ii below.

During CV and CP measurements, stirring was performed using a magnetic stirrer (stirrer rod dimensions: 30×6 mm) at a stirring speed of 550 min^{-1}. All electrochemical data were recorded digitally using a Potentiostat Interface 1000 from Gamry Instruments (Warminster, PA 18974, USA) connected to a personal computer. At the end of the polarization experiments, the electrodes were removed from the electrolyte, washed with deionized water and dried in an oven at 315 K for 24 h. The weight was again determined using a precision balance (Sartorius 1712, 0.01 mg accuracy) to check the weight loss that occurred during CP activation (60 600 s of CP).

In order to determine the wear of the anode when used as an OER electrode at constant current density, complementary CP experiments were started after completion of the electrode/electrolyte activation, so that at the end of the 60 600 s of CP (Figure 1a, black curve), the anode was removed from the electrolyte, dried and weighed before continuing the CP test. For this purpose (after completing the standard current protocol in a glass beaker), both activated electrolytes were transferred into the electrolysis cell (Figure 3). CV's were recorded at a scan rate of 20 mV s^{-1} with a step size of 2 mV.

The determination of the Faradaic efficiency for OER (method i; Figure 2) was carried out in close accordance with the procedure described in our previous paper.[25] The electrolyte used for this determination was prepared by adding 145 g NiO to 1.82 L of 0.5 M H_2SO_4. CP activation was performed using the standard current protocol (10 000 s at 150 mA cm^{-2}; 600 s at 75 mA cm^{-2} and 50 000 s at 30 mA cm^{-2}). The actual FE measurement was performed at the end of the CP activation procedure. FE was determined by performing a CP experiment at a constant current density of 30 mA cm^{-2} (total current: 60 mA). At the beginning of the dissolved oxygen monitoring (t = 0 s), the oxygen content was 0.24 mg L^{-1}. After 2182 s of CP, 2.23 mg L^{-1} oxygen was measured in the electrolyte. For details, see the caption in Figure 2.

Determination of Faradaic efficiency for OER (method ii; Figure 3, Table 1)

The charge to hydrogen and charge to oxygen conversion rates were determined by collecting both gases produced during water electrolysis at constant current density (I = 300 mA; j = 150 mA cm^{-2}). As with method i, the Faraday efficiency was determined after completion of the CP activation procedure (standard current protocol; 60 600 s of CP Figure 1a black curve). The activation procedure was carried out in two separate glass beakers, each containing 105 mL of 0.5 M H_2SO_4 and 8.4 g of NiO. Method ii was carried out in a home-made acrylic glass electrolysis cell equipped with a Nafion membrane to separate the anolyte from the catholyte (Figure 3, Video S1, Supporting Information), allowing both gases to be collected. Both anolyte and catholyte were stirred during the measurements. After completion of the standard current protocol, both activated electrolytes were transferred to the electrolysis cell (Figure 3) and the amount of oxygen and hydrogen gas produced during electrolysis at a current density of 150 mA cm^{-2} was determined (Table 1). Three experiments were carried out according to method ii and the deviations obtained in terms of cell voltage, OER potentials and OER FE and HER FE were marginal (Table 1). Note: we did not pay particular attention to keeping the distance between the electrodes as small as possible (no zero-gap

conditions). Nevertheless, a very low cell voltage of 1.35 V was obtained at $j = 10$ mA cm^{-2}. The FE for the OER was 91%–99%, and the corresponding value for the HER is $\approx$80% (Table 1), assuming a common direct oxidation of water molecules (two-electron process according to $H_2O \rightarrow H_2 + 0.5 O_2$).

Quantum Mechanical Calculations: The first-principles calculations were performed using the Vienna ab initio simulation package in which the projector augmented wave method is implemented.[1,2] Throughout the calculations, exchange-correlation interactions were approximated by the Perdew–Burke–Ernzerh generalized gradient approximation (GGA-PBE, ref. [3]). For atomic optimization, a kinetic energy cut-off of 520 eV for the plane wave, energy and force convergence criteria of 1×10^{-5} eV and 0.02 eV Å^{-1}, respectively, were employed. The surface structure was modeled by creating a super-cell with atomic slabs, each separated by a 15-Å-thick vacuum layer. Note that both models presented NiO-terminated surfaces.

Supporting Information

Supporting Information is available from the Wiley Online Library or from the author.

Conflict of Interest

The authors declare no conflict of interest.

Data Availability Statement

The data that support the findings of this study are available in the supplementary material of this article.

[1] J. Gregus, J. Guillebaud, *Eur J Contracept Reprod Health Care* **2020**, *25*, 409.

[2] J. Bongaarts, B. C. O'Neill, *Science* **2018**, *361*, 650.

[3] M. Chatenet, B. G. Pollet, D. R. Dekel, F. Dionigi, J. Deseure, P. Millet, R. D. Braatz, M. Z. Bazant, M. Eikerling, I. Staffell, P. Balcombe, Y. Shao-Horn, H. Schäfer, *Chem. Soc. Rev.* **2022**, *51*, 4583.

[4] H. Schäfer, M. Chatenet, *ACS Energy Lett.* **2018**, *3*, 574.

[5] F. Dionigi, P. Strasser, *Adv. Energy Mater.* **2016**, *6*, 1600621.

[6] S. Anantharaj, S. Rao Ede, K. Sakthikumar, K. Karthick, S. Mishra, S. Kundu, *ACS Catal.* **2016**, *6*, 8069.

[7] O. Schmidt, A. Gambhir, I. Stafell, A. Hawkes, J. Nelson, S. Few, *Int. J. Hydrogen Energy* **2017**, *42*, 30470.

[8] C. Santoro, A. Lavacchi, P. Mustarelli, V. Di Noto, L. Elbaz, D. R. Dekel, F. Jaouen, *ChemSusChem* **2022**, *15*, 202200027.

[9] H. Schäfer, D. M. Chevrier, P. Kuepper, P. Zhang, J. Wollschläger, D. Daum, M. Steinhart, C. Hess, U. Krupp, K. Müller-Buschbaum, *Energy Environ. Sci.* **2016**, *9*, 2609.

[10] H. Schäfer, K. Kuepper, K. M. Müller-Buschbaum, D. Daum, M. Steinhart, J. Wollschläger, U. Krupp, M. Schmidt, W. Han, J. Stangl, *Nanoscale* **2017**, *9*, 17829.

[11] H. Schäfer, K. Kuepper, M. Schmidt, K. Müller-Buschbaum, J. Stangl, D. Daum, M. Steinhart, C. Schulz-Kölbel, W. Han, J. Wollschläger, U. Krupp, P. Hou, X. Liu, *Catal. Sci. Technol.* **2018**, *8*, 2104.

[12] C. C. L. McCrory, S. Jung, I. M. Ferrer, S. M. Chatman, I. C. Peters, *J. Am. Chem. Soc.* **2015**, *137*, 4347.

[13] N. Danilovicet, R. Subbaraman, K.-C. Chang, S. H. Chang, Y. I. Kang, J. Snyder, A. P. Paulikas, D. Strmcnik, Y.-T. Kim, D. Myers, V. R. Stamenkovic, N. M. Markovic, *J. Phys. Chem. Lett.* **2014**, *5*, 2474.

[14] T. Reier, M. Oezaslan, P. Strasser, *ACS Catal.* **2012**, *2*, 1765.

[15] K. Sardar, E. Petrucco, C. I. Hiley, J. D. B. Sharman, P. P. Wells, A. E. Russell, R. J. Kashtiban, J. Sloan, R. I. Walton, *Angew. Chem., Int. Ed.* **2014**, *53*, 10960.

[16] T. Audichon, S. Morisset, T. W. Napporn, K. B. Kokoh, C. Comminges, C. Morais, *ChemElectroChem* **2015**, *2*, 1128.

[17] L. C. Seitz, C. F. Dickens, K. Nishio, Y. Hikita, J. Montoya, A. Doyle, C. Kirk, A. Vojvodic, H. Y. Hwang, J. K. Norskov, T. F. Jaramillo, *Science* **2016**, *353*, 1011.

[18] P. A. DeSario, C. N. Chervin, E. S. Nelson, M. B. Sassin, D. R. Rolison, *ACS Appl. Mater. Interfaces* **2017**, *9*, 2387.

[19] A. L. Strickler, D. Higgins, T. F. Jaramillo, *ACS Appl. Energy Mater.* **2019**, *2*, 5490.

[20] M. Huck, L. Ring, K. Küpper, J. Klare, D. Daum, H. Schäfer, *J Mater Chem* **2020**, *8*, 9896.

[21] H. Schäfer, K. Kuepper, J. Koppe, P. Selter, M. Steinhart, M. R. Hansen, D. Daum, *ACS Catal.* **2018**, *8*, 10914.

[22] N. Akbari, M. M. Najafpour, *Inorg. Chem.* **2023**, *62*, 19107.

[23] L. Yang, G. Yu, X. Ai, W. Yan, H. Duan, W. Chen, X. Li, T. Wang, C. Zhang, X. Huang, J.-S. Chen, X. Zou, *Nat. Commun.* **2018**, *9*, 5236.

[24] L. C. Seitz, C. F. Dickens, K. Nishio, Y. Hikita, J. Montoya, A. Doyle, C. Kirk, A. Vojvodic, H. Y. Hwang, J. K. Norskov, T. F. Jaramillo, *Science* **2016**, *353*, 1011.

[25] H. Schäfer, S. Sadaf, L. Walder, K. Kuepper, S. Dinklage, J. Wollschläger, L. Schneider, M. Steinhart, J. Hardege, D. Daum, *Energy Environ. Sci.* **2015**, *8*, 2685.

[26] S. Brunauer, P. H. Emmett, E. Teller, *J. Am. Chem. Soc.* **1938**, *60*, 309.

[27] M. E. C. Pascuzzi, M. van Velzen, J. P. hofmann, E. J. M. Hensen, *ChemCatChem* **2021**, *13*, 459.

[28] Y. Xue, J. Fang, X. Wang, X. Xu, Y. Zhang, Q. Lv, M. Liu, W. Zhu, Z. Zhuang, *Adv. Funct. Mater.* **2021**, *31*, 2101405.

[29] W. Zhao, F. Xu, Z. Wang, Z. Pan, Y. Ye, S. Hu, B. Weng, R. Zhu, *Small* **2022**, 2205495.

[30] M. Ji, X. Yang, S. Chang, W. Chen, J. Wang, D. He, Y. Hu, Q. Deng, Y. sun, B. Li, J. Xi, T. Yamada, J. Zhang, H. Xiao, C. Zhu, J. Li, Y. Li, *Nano Res.* **2022**, *15*, 1959.

[31] C. Klewe, M. Meinert, A. Boehnke, K. Kuepper, E. Arenholz, A. Gupta, J. M. Schmalhorst, T. Kuschel, G. Reiss, *J. Appl. Phys.* **2014**, *115*, 123903.

[32] S. Uhlenbrock, C. Scharfschwerdt, M. Neumann, G. Illing, H. J. Freund, *J. Phys.: Condens. Matter* **1992**, *4*, 7973.

[33] M. C. Biesinger, B. P. Payne, A. P. Grosvenor, L. W. M. Lau, A. R. Gerson, R. S. C. Smart, *Appl. Surf. Sci.* **2011**, *257*, 2717.

[34] M. C. Biesinger, L. W. M. Lau, A. R. Gerson, R. S. C. Smart, *Phys. Chem. Chem. Phys.* **2012**, *14*, 2434.

[35] H. Schäfer, D. M. Chevrier, P. Zhang, J. Stangl, K. Müller-Buschbaum, J. D. Hardege, K. Kuepper, J. Wollschläger, U. Krupp, S. Dühnen, M. Steinhart, L. Walder, S. Sadaf, M. Schmidt, *Adv. Funct. Mater.* **2016**, *26*, 6402.

ADVANCED
SCIENCE NEWS

www.advancedsciencenews.com

NANO · MICRO
small
www.small-journal.com

[36] S. Lee, Y.-C. Chu, L. Bai, H. M. Chen, X. Hu, *Chem Catal* **2023**, *3*, 100475.

[37] A. P. Grosvenor, B. A. Kobe, M. C. Biesinger, N. S. McIntrye, *Surf. Interface Anal.* **2004**, *36*, 1564.

[38] R. K. Venkateswara, C. S. Sunandana, *J. Nanosci. Nanotechnol.* **2008**, *8*, 4247.

[39] C. B. Azzoni, A. Paleari, V. Massarotti, D. Capsoni, *J. Phys.-Condens. Mat.* **1996**, *8*, 7339.

[40] P. Ganguly, V. Raamaswamy, I. S. Mulla, R. F. Shinde, P. P. Bakare, S. Ganapathy, P. R. Rajamohanan, N. V. K. Prakash, *Phys. Rev. B* **1992**, *46*, 11595.

[41] R. Stoyanova, E. Zhecheva, S. Angelov, *Solid State Ion* **1993**, *59*, 17.

[42] R. Stoyanova, E. Zhecheva, C. Friebel, *J Phys Chem* **1993**, *54*, 9.

[43] R. Stoyanova, E. Zhecheva, C. Friebel, *Solid State Ion* **1994**, *73*, 1.

[44] I. Yamada, K. Ubukoshi, K. Hirakawa, *J. Phys. Soc. Japan* **1985**, *54*, 3571.

[45] K. Hirota, Y. Nakazawa, M. Ishikawa, *J. Phys.: Condens. Matter* **1991**, *3*, 4721.

[46] K. J. Tielrooij, N. Garcia-Araez, M. Bonn, H. J. Bakker, *Science* **2010**, *328*, 1006.

[47] F. Perakis, L. De Marco, A. Shalit, F. Tang, Z. R. Kann, T. D. Kühne, R. Torre, M. Bonn, Y. Nagata, *Chem. Rev.* **2016**, *116*, 7590.

[48] H. Schäfer, A. Schuster, S. Kunis, T. Bookholt, J. Hardege, K. Ruewe, J. Brune, *Adv. Mater.* **2023**, *35*, 2300099.

[49] I. Leonov, S. Biermann, *Phys. Rev. B* **2021**, *103*, 165108.

[50] L. Trotochaud, S. L. Young, J. K. Ranney, S. W. Boettcher, *J. Am. Chem. Soc.* **2014**, *136*, 6744.

[51] J.-J. Lv, J. Zhao, H. Fang, L.-P. Jiang, L.-L. Li, J. Ma, J.-J. Zhu, *Small* **2017**, *13*, 1700264.

[52] J. Zhang, Q. Zhang, X. Fen, *Adv. Mater.* **2019**, *31*, 1808167.

[53] Y. Xu, W. Tu, B. Zhang, S. Yin, Y. Huang, M. Kraft, R. Xu, *Adv. Mater.* **2017**, *29*, 1605957.

[54] C. Lyu, Y. Li, J. Cheng, Y. Yang, K. Wu, J. Wu, H. Wang, W.-M. Lau, Z. Tian, N. Wang, J. Zheng, *Small* **2023**, *19*, 2302055.

[55] P. Wang, Y. Luo, G. Zhang, M. Wu, Z. Chen, S. Sun, Z. Sh, *Small* **2022**, *18*, 2105803.

[56] Y. Wei, L. Yi, R. Wang, J. Li, D. Li, T. Li, W. Sun, W. Hu, *Small* **2023**, *19*, 2301267.

[57] X. Guo, M. Li, L. Qiu, F. Tian, L. He, S. Geng, Y. Liu, Y. Song, W. Yang, Y. Yu, *Chem. Eng. J.* **2023**, *453*, 139796.

[58] A. Ali, F. Long, P. K. Shen, *Electrochem. Energy Rev.* **2022**, *5*, 1.

[59] P. Wang, Y. Luo, G. Zhang, Z. Chen, H. Ranganathan, S. Sun, Z. Shi, *Nano-Micro Lett.* **2022**, *14*, 120.

[60] Y. Guo, T. Park, J. W. Yi, J. Henzie, J. Kim, Z. Wang, B. Jiang, Y. Bando, Y. Sugahara, J. Tang, Y. Yamauchi, *Adv. Mater.* **2019**, *31*, 1807134.

[61] Y. Mu, T. Wang, J. Zhang, C. Meng, Y. Zhang, Z. Kou, *Electrochem. Energy Rev.* **2022**, *5*, 145.

[62] DIN ISO 9277:2014-01, Bestimmung der spezifischen Oberfläche von Festkörpern mittels Gasadsorption – BET-Verfahren (ISO 9277:2010), Beuth Verlag GmbH, Berlin.